Energy & Environmental Science

A single-site iron catalyst with preoccupied active center that achieves selective ammonia electrosynthesis from nitrate

Journal:	*Energy & Environmental Science*
Manuscript ID	EE-ART-02-2021-000545.R1
Article Type:	Paper
Date Submitted by the Author:	04-Apr-2021
Complete List of Authors:	Li, Panpan; The University of Texas at Austin, Department of Mechanical Engineering Jin, Zhaoyu; University of Texas at Austin College of Natural Sciences, Department of Chemistry Fang, Zhiwei; The University of Texas at Austin, Materials Science and Engineering Yu, Guihua; The University of Texas at Austin, Materials Science and Engineering

PAPER

Received 00th January 20xx,

Accepted 00th January 20xx

DOI: 10.1039/x0xx00000x

A single-site iron catalyst with preoccupied active center that achieves selective ammonia electrosynthesis from nitrate

Panpan Li,[a] Zhaoyu Jin,[b]* Zhiwei Fang,[a] and Guihua Yu[a]*

The necessity to pursue sustainable ammonia (NH_3) production with economic and environment-friendly technologies is growing with the global development aim of future fertilizer and renewable energy industries. Electrosynthesis of ammonia from nitrate reduction is encouraging for both environmental nitrogen pollution management and artificial nutrient recycling. However, it is fundamentally difficult to regulate reaction pathways for the efficient and selective ammonia production over competing reactions, e.g., hydrogen evolution reaction, particularly under aqueous conditions. Enlightened by the unique and tunable local electronic structures, an iron-based single-atom catalyst is reported in this contribution. We demonstrate a polymer-hydrogel strategy for preparing the nitrogen-coordinated Fe sites with uniform atomic dispersion on carbon. The catalyst exhibits a maximum NH_3 yield rate of 2.75 mg_{NH3} h^{-1} cm^{-2} (ca. 30 mol_{NH3} h^{-1} g_{Fe}^{-1}) with nearly 100% faradaic efficiency. Furthermore, the catalytically active individual, Fe site, in isolated atom state displays twelve times higher turnover frequency than that in metallic Fe nanoparticles. Experimental evidence suggests the single-site iron would experience a nitrate-preoccupied transition center, which prohibits water adsorption as the competitive reaction that generally exists for bulk catalysts. Theoretical insights into the localized structure further assist a better understanding and support of the high selectivity for NH_3 achieved by the Fe single-atom catalyst.

Broader Context

Renewable energy powered low-temperature electrification of ammonia production as an alternative to the Haber–Bosch process could eliminate the use of fossil fuels and the discharge of CO_2 emissions. Direct electroreduction of dinitrogen has emerged as an attractive technique in recent years, while to date it typically only allows to produce limited quantities of NH_3 with poor selectivity. Here an electrochemical strategy is introduced to efficiently produce NH_3 from nitrate driven by an earth-abundant iron single-site catalyst. The nitrate, long considered to be a toxic contaminant in industrial and agriculture wastewater, is thus a valuable resource to be recovered and used to produce NH_3. However, it is fundamentally difficult to control reaction pathways to advance the yield and selectivity over competing reactions, such as hydrogen evolution, under aqueous conditions. This work found that Fe single atoms could experience a nitrate-preoccupied mechanism during the catalysis, which effectively prohibited the competitive water adsorption.

Introduction

The manufacture of ammonia has seen rapid growth in tonnage globally and becomes one of the most central productions in chemical industries since the past century.[1] The invention of the Haber–Bosch (H-B) process, which converts atmospheric nitrogen gas (N_2) and hydrogen (H_2) to NH_3, allows the booming development of modern agriculture with synthetic nitrogen fertilizers.[2, 3] In addition, ammonia has been regarded as a renewable energy carrier as a consequence of primary benefits, including the high energy density, carbon-free, safe, and cost-effective transportation.[4, 5] Despite the continued technological advancement of the H-B process, there is an urgent need to address the substantial energy consumption and huge greenhouse emission, which has been beyond any other industrial chemical-making reactions.[6] Lately, increasing attention has been paid to an alternative approach, aqueous-based electrosynthesis of ammonia from N_2 under ambient conditions.[7] However, this process suffers from poor efficiency because of difficulties in breaking the triple bond of N_2 and the suppression of the hydrogen evolution reaction (HER).[8-11] Another oxidized form of nitrogen, nitrate (NO_3^-), ubiquitously exists in the environment as the result of anthropogenic forcing on soil and water pollution through crop fertilization. The NO_3^- has long been concerned as a toxic contaminant, which is strictly controlled under the safe level in emissions.[12] There is a surge in expenditure for the management of nitrogen pollution worldwide over the past several decades.[13, 14] Though ammonia is considered as the upstream

[a] Materials Science and Engineering Program, Texas Materials Institute, The University of Texas at Austin, Austin, Texas 78712, United States.
[b] Center for Electrochemistry, Department of Chemistry, The University of Texas at Austin, Austin, Texas 78712, United States.

Electronic Supplementary Information (ESI) available: SI-SECM tests details; calculation and computational details; SEM images; XPS spectra; fitting results of EXAFS; calibration curves and quantification of products; 1H NMR and 15N label-ling tests; electrochemical measurements; SI-SECM analysis. See DOI: 10.1039/x0xx00000x

product of nitrate in industry, the electrochemical conversion of nitrate to NH_3 has been receiving renewed interest since the past year.[15, 16] The basic motivation of converting nitrate to ammonia is to develop a sustainable route that permits nitrogen nutrient/fuel recovery from wastewater with clean water production. As such, one would expect the nitrogen in wastewater and soil to be no longer an environmental burden, but as a resource for fertilizer recycling. The process is analogous to the microbially dissimilatory nitrate reduction to ammonium, which acts as an important role for the terrestrial and oceanic nitrogen cycle sustainability.[17]

Nitrate is in principle more reactive than dinitrogen to be reduced to ammonia with a favorable thermodynamic potential (0.69 V vs. RHE) under alkaline conductions.[18] However, the electrochemical nitrate reduction reaction (NitRR), involves eight-electron and nine-proton transfer, and thus markedly lowers the overall kinetic rate. This is particularly disadvantageous to the operation under aqueous conditions on account of the HER competing for active sites. Besides, complicated products of the NitRR, possibly including NO_2^-, N_2, and NH_3, also raise major challenges for the goal of highly selective synthesis. To address these issues, single-atom catalysts (SACs) have emerged as a promising type of catalyst with much higher atomic utilization, distinct activity, and selectivity in comparison to bulk structures, showing great potential in effective nitrate-to-ammonia synthesis.[19] Interestingly, the isolated site with a unique and tunable localized coordination state permits one to highly selectively adsorb specific substance.[20, 21] While several previous publications have demonstrated this feature in catalyzing some reactions, research has yet to extend the potential capability of SACs to the NitRR.[22-24] Besides, an understanding of their selectivity largely relied on the theoretical modeling which was adopted by most studies with a lack of experimental validation.[19, 25] Indeed, techniques traditionally employed to characterize ensemble materials are only able to provide limited information on SACs because of the less accessible active species. The complexity of NitRR as stated also leaves a major challenge to empirical evidence of the catalytic behavior of individual sites.

In nature, microbial nitrate and nitrite reductases have been recognized as the most efficient species for the reduction of nitrogen-containing oxyanions during anaerobic respiration.[26, 27] Ferredoxin-dependent nitrite reductase widely found in biological green alga and cyanobacteria can actively produce ammonia through the photosynthetic nitrate assimilation pathway.[28] Inspired by the single-site of iron, here we reported a densely populated Fe single-atom catalyst derived from a ferric acetylacetonate/polypyrrole hydrogel precursor, which demonstrated an impressive selectivity and activity for the electrocatalytic NitRR under alkaline conditions. Zero-valence iron has been reported as an effective catalyst to remove nitrate in water for managing the nitrogen pollution. However, the metallic surface suffers from the problematic oxidation, which forms iron oxide with poor conductivity and activity. In the case of isolated Fe sites, the catalyst displays nearly 100% selectivity for producing ammonia and the turnover frequency that is over twelve times as high as that of Fe nanoparticles. The mechanistic insight reveals a preoccupation of nitrate on Fe(II)-N_x may warrant the specificity of the nitrate-to-ammonia process, while the classical site-competition between the NitRR and HER was observed for the bulk Fe. The study presents an important instance of recently concerned and featured SACs and will contribute to a deeper understanding of intrinsic catalytic behavior on isolated site.

Experimental

Preparation of SDS induced PPy (PPy-SDS) hydrogels

PPy-SDS hydrogels were synthesized using surfactants as soft templates.[29] Specifically, solution A was prepared by dissolving pyrrole monomers (416 μL, 0.3 M) and sodium dodecyl sulfate (SDS, 0.58 g, 0.1 M) into deionized (DI) water (10 mL) with the ultrasonic treatment. Then, ammonium peroxydisulfate (APS, 1.5 g, 0.3 M) was dissolved into DI water (10 mL) marked as solution B. After cooling to room temperature, solution A and solution B were quickly mixed and rested for at least 1 h to sufficient polymerization. The as-prepared PPy-SDS hydrogels were purified by DI water to eliminate the unreacted residual chemicals.

Preparation of Fe-PPy single-atom catalysts and PPy-SDS derived carbon materials

The purified PPy-SDS hydrogels were directly added into iron(III) acetylacetonate ($Fe(acac)_3$) ethanol solution (0.05 M, 40 mL) for 10 h stirring. Then, Fe-PPy hydrogels were washed with ethanol for several times and dried in vacuum at 30 °C overnight. After grounded into uniform powders, Fe-PPy hydrogels were heated to 800 °C with 10 °C min^{-1} and kept for 2 h in an argon flow. Then, samples were naturally cooled to room temperature and further immersed in 0.5 M H_2SO_4 solution for 8 h to remove the aggregated clusters and particles. Samples were subsequently washed with DI water until reaching neutral pH and dried in vacuum at 80 °C. The second pyrolysis under the same conditions was carried out to reduce inactive Fe sites in catalysts after the acidic treatment[30] and finally produce Fe-PPy SACs. PPy-SDS derived carbon materials (denoted as PPy) were obtained by directly calcinating PPy-SDS hydrogels under the same conditions.

Characterizations

The field emission Hitachi S5500 microscope (Japan) was employed to acquire scanning electron microscopy (SEM) images. The high-angle annular dark-field scanning transmission electron microscopy (HAADF-STEM) images and energy-dispersive X-ray spectroscopy (EDS) images were conducted with a JEOL NEOARM probe-corrected transmission electron microscope with aberration correction (Japan). X-ray absorption fine structure spectra (XAFS) analysis, including the X-ray absorption near edge structure (XANES) and extended X-ray absorption fine structure (EXAFS), were carried out at the BL14W1 beamline of the Shanghai Synchrotron Radiation Facility, China. All the samples were characterized using Fe-K edge XANES and EXAFS in a transmission mode under ambient conditions and Fe foil was used as references. The analysis of all XAFS data was performed using IFEFFIT. The total Fe contents of samples were obtained via a THERMO VG PQ ExCell quadrupole based inductively coupled plasma mass spectrometer (ICP-MS, USA) with diluted samples dissolved in 2% HNO_3 (ion concentration below 200 ppm). X-ray photoelectron spectra (XPS) were acquired with Kratos Axis Ultra DLD photoelectron spectroscopy (UK). All binding energies were referenced to C 1s peak at 284.6 eV to correct the possible shift. ^{57}Fe Mössbauer spectroscopy was obtained with a Rh/^{57}Co source at room temperature using an α-Fe foil as the velocity calibration.

Ultraviolet-visible (UV-Vis) absorption spectra were recorded by a Thermo Evolution 300 spectrophotometer (the USA). All ^{1}H nuclear magnetic resonance (^{1}H NMR) spectra were collected on Varian VNMRS 600 MHz (the USA) with water suppression.

Electrochemical measurements

Nitrate reduction reaction activities were carried out on a BioLogic multi-channel potentiostat (VMP-3 model, France) equipped with a sealed H-shape electrochemical cell separated by Nafion 115 membrane. Prior to all tests, Nafion membrane was treated with H_2O_2 (5 wt%) aqueous solution at 80 °C for 1 h and ultrapure water at 80 °C for another 1 h, respectively. Catalysts ink was prepared by adding 4 mg catalyst powder to DI water-isopropyl alcohol (500 µL, 3:1in v/v) and Nafion solution (20 µL, 5 wt%, Dupont, USA) with the ultrasonic treatment. Fe nanoparticles (30-50 nm) were purchased from Sigma-Aldrich (USA). The uniform catalyst ink was drop-casted on carbon paper (the active area: 0.5×0.5 cm^2) with a mass loading of ca. 240 µg cm^{-2} unless specified. The carbon paper with loading catalysts was directly used as the working electrode, while an Ag/AgCl (1 M KCl) and a graphite rod were employed as the reference and counter electrode, respectively. Before electrochemical measurements, electrolytes (0.1 M KOH and 0.1 M KNO_3) were degassed by ultrapure argon flow to remove O_2 and N_2. Linear sweeping voltammograms (LSVs) were obtained from -1.3 to -1.8 V vs. Ag/AgCl with a scan rate of 10 mV s^{-1}. Chronoamperometry tests were carried out at given potentials for 30 min to evaluate the yield rate and faradaic efficiency of NH_3. The potentials vs. the reversible hydrogen electrode (RHE) were obtained by transforming the recorded potentials against Ag/AgCl based on the calibration equation expressed as $E_{RHE} = 0.059 \times pH + E_{Ag/AgCl} + 0.23 = E_{Ag/AgCl} + 0.997$. Ag/AgCl electrode was examined to be stable before and after electrolysis experiments via calibrating with a home-made hydrogen electrode. Note that, the pH-dependent thermodynamic potential change (less than 1% based on the activity coefficient modification of OH^-) affected by KNO_3 is not included here.

Surface interrogation scanning electrochemical microscopy (SI-SECM) analysis was conducted on a CHI920C SECM bipotentiostat (CH Instrument, the USA). The details were described in the Supplementary Information.

Results and discussion

Preparation and characterizations

SDS-induced polypyrrole hydrogels prepared through the soft template strategy were employed as ideal precursors of carbon support for loading single Fe atoms due to the large surface area, derived conductive networks, and abundant dopants.[31-33] Specifically, pyrrole monomers, sodium dodecyl sulfate, and DI water were thoroughly mixed to generate the oil-in-water emulsion droplets as shown in Scheme 1. Then, sulfate groups on the droplet electrostatically adsorbed the dissolved pyrrole on its surface and formed crosslinked PPy nanoparticles with adding initiators. After rinsed, hierarchal PPy-SDS hydrogels were obtained by removing soft templates. SDS micelles acting as the crosslinkers greatly contribute to PPy hydrogels formation (Scheme 1). As indicated in Fig. S2a and b, PPy-SDS hydrogels reveal the sheet-like porous structure from low-magnification SEM images. From the enlarged view in Fig. S2c,

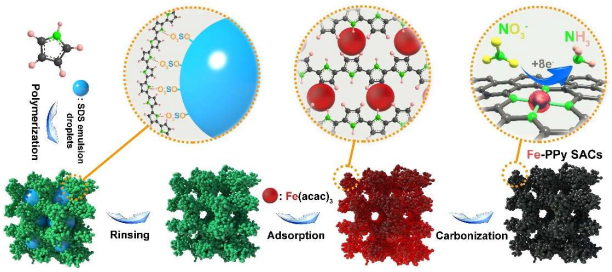

Scheme 1 The synthetic route of Fe-PPy SACs.

the porous sheets are composed of interconnected nanoparticles with reduced size (ca. 40 nm). However, PPy nanoparticles synthesized without adding SDS show a much larger size (ca. 300 nm) and no gelation was found in this process. SDS induced PPy hydrogels were proved to reveal the improved porosity and enlarged surface area.[29] Thus, PPy-SDS hydrogels could offer an increased capability to accommodate $Fe(acac)_3$ molecules via stacking interactions between the acac-type chelate rings and polymer backbones.[34] From Fig. S1b, the discoloration of $Fe(acac)_3$ solution indicates the adsorption of Fe species in PPy-SDS hydrogels. After the carbonization, Fe(III)-adsorbed PPy-SDS hydrogels were transformed to be Fe single-atom catalysts (Fe-PPy SACs) without obvious structural changes (Fig. 1a).

HAADF-STEM image (Fig. 1b) with the aberration correction reveals the isolated bright spots with a diameter of ca. 0.1 nm, which is strong evidence for observing single metal atoms. To confirm the elemental composition of these spots, the electron energy loss spectrum (EELS) was collected at a local area of one atom marked with the red circle in Fig. 1b. Fig. 1c shows iron, carbon and nitrogen elements are mainly distributed in the selected region. Moreover, XPS further confirm the presence of C, N, Fe in Fe-PPy SACs (Fig. S3a). In addition, the oxidation state of Fe is +2 based on the binding energy of ca. 711 eV from Fig. S3b.[35, 36] Metal coordination nitrogen at ca. 399 eV (Fig. S3c) exhibits the formation of Fe-N species.[37] However, XPS analysis is far from satisfactory for confirming the fine structure of single atom materials because of the low content of Fe species (2.38 wt% from ICP-MS). Thus, the Mössbauer spectrum in Fig. 1d was carried out to figure out the configuration of iron species. As a result, the transmission profile of Fe sites in Fe-PPy SACs is mainly deconvoluted as D1 and D2 doublets, suggesting Fe atom is likely to be coordinated by four nitrogen atoms. For the dominant D1 configuration, the Fe atom is slightly out of the planar surface, and two empty d bands are in the low spin state.[38, 39] D1 configuration was proved to perform better adsorption, such as O_2, as a result of the partially filled d_{z2} band.[40]

To detail more precise structural information, XAFS were conducted for determining the interaction between the Fe atom and other elements. Fig. 1e compares Fe K-edge XANES of Fe foil, Fe_2O_3, and Fe-PPy SACs. Fe-PPy SACs show the adsorption intensity at rising-edge position of ca. 7120 eV is located between Fe foil and Fe_2O_3, suggesting the oxidation state of iron is close to +2, consistent with the result from XPS. The obvious pre-edge peak at ca. 7113.5 eV for Fe-PPy is in good agreement with the typical Fe-N_4 configuration.[41] The Fourier transform of EXAFS (FT-EXAFS) in Fig. 1f confirms Fe atom is mainly coordinated with N atoms (Fe-N bond at 1.55 Å) rather than other Fe atoms (Fe-Fe bond at ca. 2.20 Å) in line with the atomically

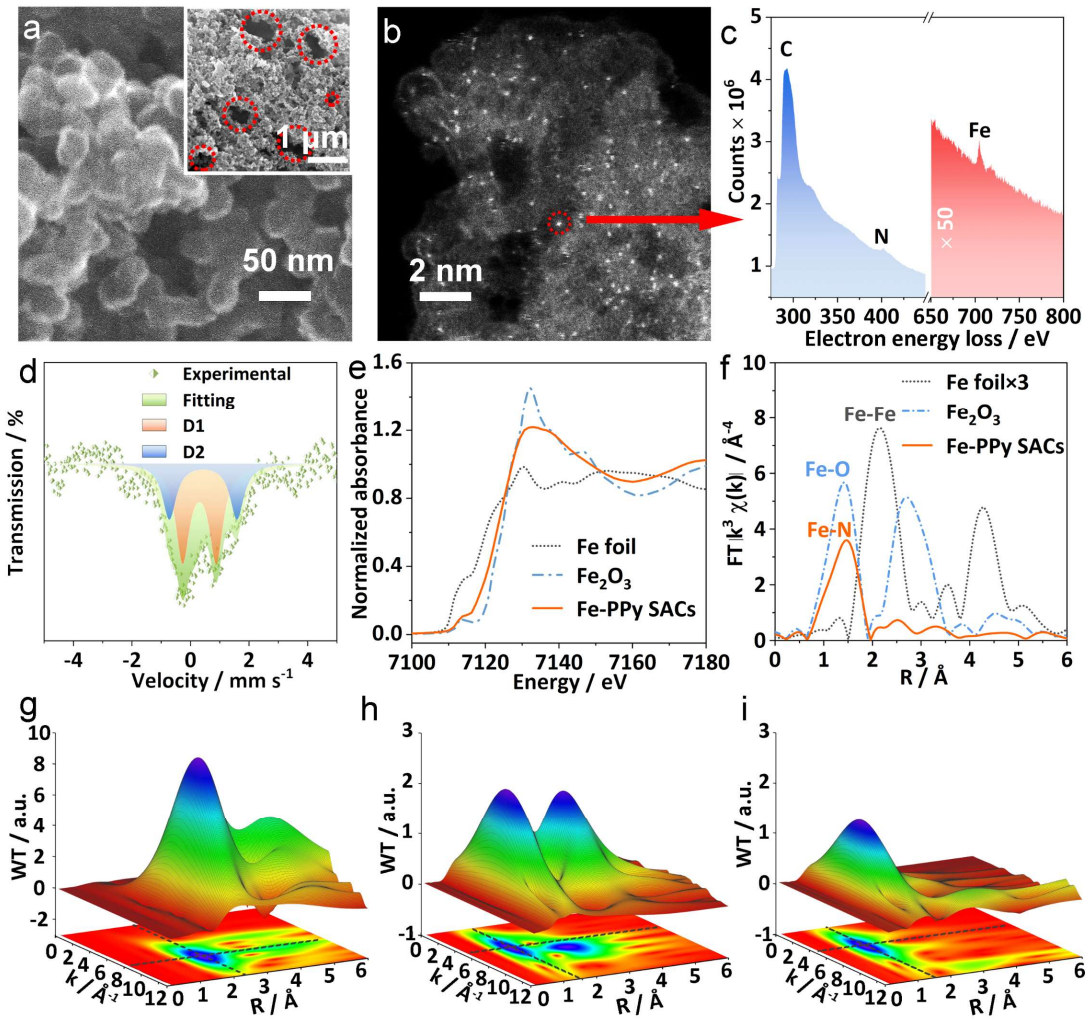

Fig. 1 The morphology and compositions of Fe-PPy SACs. (a) SEM and (b) HAADF-STEM images of Fe-PPy SACs. (c) The local EELS of the isolated Fe site. (d) Mössbauer spectrum of Fe-PPy SACs. (e) XANES and (f) FT-EXAFS of samples. WT plots of (g) Fe foil, (h) Fe_2O_3, and (i) Fe-PPy SACs based on EXAFS.

dispersed Fe sites of Fe-PPy SACs.[42] Based on Mössbauer and FT-EXAFS, the Fe-N_4 model structure (Fig. S4a) was proposed here as the single-site feature in the pristine catalyst and was subsequently employed to fit the FT-EXAFS spectrum. As indicated in Fig. S4b-c, EXAFS fitting curves can well fit with the experimental curves in k and R spaces. According to the fitting results in Table S1, the coordination number was obtained to be ca. 3.8 and bonding length was ca. 1.980 nm. To better visualize EXAFS spectra of Fe foil, Fe_2O_3, and Fe-PPy SACs, wavelet transform (WT) plots (Fig. 1g-i) were processed based on the values of k and R spaces. The contour graph (below) is the projection of a three-dimensional (3D) surface (above). For the case of Fe-PPy SACs, only one main peak belonging to the Fe-N bond is located at 4-6 $Å^{-1}$ and 1-2 Å, showing a slight difference compared with the Fe-O bond in Fe_2O_3. Another strong peak of Fe_2O_3 is similar to metallic Fe, which is ascribed to Fe-Fe shell in oxides.[27]

Electrocatalytic performance for NitRR

LSV curves for PPy derived carbon materials (denoted as PPy), Fe nanoparticles (Fe NPs, 30-50 nm), and Fe-PPy SACs were recorded in Fig. 2a. Before adding NO_3^-, we can clearly observe catalytic current onset after ca. -0.3 V for the HER, while current densities for all samples show a remarkable increase with adding 0.1 M NO_3^-. Moreover, a positive shift in potentials is also noticed, particularly for the catalysts with Fe. A small reduction peak at ca. -0.2 V on Fe-PPy SACs is due to the diffusion control of NO_3^- reduction. The charge transfer number (n) of this peak was determined to be ca. 8 via the relationship between the peak current and the scan rate under 10 mM NO_3^- concentration (a diffusion-control condition) as shown in Fig. S5. It suggests the high efficiency of ammonia production at -0.2 V. To further confirm the NitRR ability at low overpotentials, current density–time (I–t) curves before and after introducing 0.1 M NO_3^- were recorded (the inset of Fig. 2b). Only Fe-PPy SACs deliver obvious cathodic current response at 0, 0.1, and 0.2 V upon adding nitrate, while no such signals have ever been seen in all trials under the same conditions for other samples.

The well-established indophenol blue spectrophotometric method was used to quantify the produced ammonia in electrolytes, further determining the yield rate (Y.R.) and faradaic efficiency (F.E.) of NH_3 (see calculation details in Supplementary Information). The reliability of this method and the origin of ammonia were confirmed via ^1H NMR (see more details in Fig. S8). The results indicate the produced ammonia is mainly from electrocatalytic NO_3^- reduction rather than the interference from the environment and catalysts themselves. To better illustrate the NitRR performance of studied catalysts, yield rates at low and high overpotentials (Fig. 2b and 2c) were plotted, separately. For Fe-PPy SACs, ammonia can be produced from 0.2 V with a Y.R. of ca. 1.3 μg_{NH3} h^{-1} cm^{-2} and an F.E. of ca. 20% (Fig. 2d). As the comparison, for PPy and Fe NPs, NH_3 can be only found at potentials lower than 0 V. In all of the experiments, Fe-PPy SACs outperform other samples and reach ca. 2.75 mg_{NH3} h^{-1} cm^{-2} at -0.7 V and nearly 100% in F.E. after -0.3 V. In contrast, PPy shows the relatively inferior NitRR activity with less than 0.62 mg_{NH3} h^{-1} cm^{-2} and 47%, implying isolated Fe sites on Fe-PPy SACs make a prominent contribution to the electrocatalytic nitrate reduction to ammonia. Though Fe NPs achieve a high Y.R. of ca. 3.0 mg_{NH3} h^{-1} cm^{-2}, the corresponding F.E. is less than 80%. It is probably due to the intense competition from the HER on iron nanoparticles as we could observe some bubbles during electrolysis. No or very little gas was found, by comparison, on Fe-PPy SACs at any given potentials as demonstrated.

Other products of NitRR typically involve complicated nitrogen-containing species, such as NO_2^-, N_2, and NO_x, accompanying with the HER as the competitive reaction at negative potentials. In this regard, it is of necessity to determine the other possible products for better interpreting the superior selectivity of single-atom catalysts. One impressive finding is that almost no H_2 (F.E. < 2%) is detected in Fe-PPy SACs (Fig. S9f). In contrast, Fe NPs (Fig. S9g) and PPy (Fig. S9h) appear to experience the noticeable H_2 evolution starting from -0.3 V, reaching the highest F.E.(H_2) of ca. 22% and ca. 35%, respectively. NO_2^- is the essential intermediate of NitRR and is almost detectable in three catalysts at all potential ranges, while F.E.(NO_2^-) is much less than F.E.(NH_3). For Fe-PPy SACs, F.E.(NO_2^-) is less than < 10%, which is much lower than other reported electrocatalysts.[15, 25] F.E.(others) is defined as the F.E. of remaining products (e.g., N_2, N_2H_4, NO_2) apart from F.E.(NH_3), F.E.(NO_2^-), and F.E.(H_2). Since current densities at potential above 0 V are too low (microamp level), F.E.(others) remains significant deviations from background signals, double-layered charging current, and instrumental offset, which would not contribute to any faraday reactions. Consequently, the selectivity of ammonia for the NitRR is compared from -0.1 to -0.7 V (vs. RHE) in Fig. S10d, where Fe-PPy SACs reveal the impressively selective NH_3 production with over 80% at all potentials.

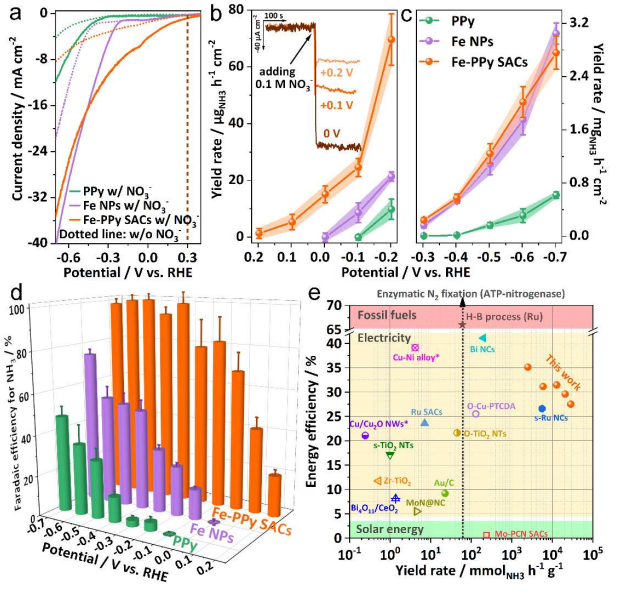

Fig. 2 Electrocatalytic activities of different catalysts for the NO_3^- reduction to NH_3. (a) LSVs of Fe-PPy SACs, Fe NPs, and PPy with and without adding NO_3^- in the electrolytes. The yield rate of three catalysts at (b) low and (c) high overpotentials. (d) Faradaic efficiency for ammonia. (e) The energy efficiency and yield rate of ammonia synthesis for Fe-PPy SACs compared with the reported catalysts (see details in Table S2); The yield rate is normalized by mass loading of active species in catalysts.

The durability of Fe-PPy SACs was evaluated by yield rate and faradaic efficiency of ammonia after cyclic electrolysis (Fig. S11a), where only a slight fluctuation is observed within 10 cycles. Additionally, the accumulated charge through the catalyst results in the linear increase of ammonia yield (Fig. S11b), suggesting the stable NH_3 production with increment on the duration of electrolysis. The STEM image after the cyclic electrolysis (Fig. S12a) indicates isolated Fe atoms still exist in the carbon matrix. EELS (Fig. S12b) and EDS (Fig. S12c-d) images before and after electrolysis were carried out to confirm the stability of Fe-PPy SACs. Moreover, the faradaic efficiency can remain at above 80% within a wide range of KNO_3 concentration from 1 to 500 mM (Fig. S13). For better interpreting the merits of NitRR, we compared the energy efficiency (E.E.) and the yield rate of ammonia synthesis among five different ammonia synthesis protocols, including H-B process (☆), enzymatic N_2 fixation, photocatalytic N_2RR (□), electrocatalytic N_2RR (Δ), and electrocatalytic NitRR (○). Though the H-B process owns the highest E.E. of ca. 60%,[43] it largely relies on fossil fuels, which leads to the massive CO_2 emission. Photocatalytic N_2RR can produce ammonia directly through solar energy, while it shows a low E.E. with less than 1%.[44] Electricity can be generated from green and sustainable energy, e.g. solar energy through photovoltaic cells.

Hence, the electrification of ammonia synthesis is promising and shows a high E.E. of up to 40% (E.E. was obtained from the half-cell overpotential of the N_2RR or NitRR, assuming 1.23 V for the anodic water oxidation) even though it currently faces a relatively high energy consumption as the region marked in yellow shows. In particular, most electrocatalysts for N_2RR exhibit a low yield rate of up to 10 mmol h^{-1} g^{-1} that appears less competitive than the H-B process. By contrast, electrocatalytic NitRR presents an impressively higher yield rate and even outperforms conventional H-B process and enzymatic N_2 fixation.[45] Notably, Fe-PPy SACs in this work are recorded with the impressive performance for electrified NH_3 production among the recent reports summarized in Table S2.

Identification of the preoccupied Fe(II)-N_x site during NitRR

Several recent publications have demonstrated the SI-SECM, an in situ and quantitative technique, could afford insights into the kinetic behavior of redox species relevant to the electrocatalysis.[8, 37, 46, 47] In this work, we employed the SI-SECM to time-dependently analyze the site density of the single-site Fe moiety with dynamic oxidation state toward the nitrate reduction and water dissociation at given potentials. As shown in Fig. 3a, a catalyst powder ultramicroelectrode (UME) was prepared and severed as the substrate electrode while a similar-sized Pt UME as the tip electrode was aligned above it with the inter-electrode distance of about 2 µm. The solution with KOH as the supporting electrolyte contained a redox mediator, ferrocenemethanol (Fc), which was subsequently oxidized into the Fc^+ at the tip during the titration. The tip-generated Fc^+ can react with the Fe(II) and Fe(0) in catalysts, after which the instrument records the positive feedback on the tip current. Previous literature reported the ammonia oxidation on Pt surface would result in the dissolution of electrode.[48] Nonetheless, in the control experiment, we did not see such current feedback on the tip in the presence or absence of ammonia, where a pure Pt substrate with no Fe active sites was used.

In situ spectroscopic techniques, such as XANES, have shown the capability to investigate the dynamic oxidation state and the localized structure of catalytically active sites during catalysis.[38] Yet there are no studies that have developed nitrate-adsorbed single-site Fe-N-C models (both ad-sorbates and active moiety contain nitrogen) to allow the insight into the NitRR mechanism. The very fast reaction rate of the active intermediates would further complicate the detection and analysis. Additionally, these methods are not valid for providing quantitative site information and high time-resolution measurements of reaction kinetics. SI-SECM, a coulometric titration-based approach permits one to precisely measure the amount of charge passed to a starting catalyst layer. Fig. 3b displays the charges recorded at the tip against different potentials, which were integrated from the current-time titration curves in Fig. S14c. There are two obvious leaps, implying the oxidation state transition upon corresponding potentials. In particular, the increase of the charge at the higher potential of 0.8 ~ 0.9 V is ascribed to the reduction of Fe(III)-N_x to Fe(II)-N_x while the further transformation to Fe(0)-N_x with charges around twice larger than that of the first reduction process can be seen between 0 and -0.1 V. Here we did not specify the exact coordination number of the Fe-N_x structure as it might involve the dynamic environment under the redox conditions for the NitRR, whereas our SI-SECM is unlikely to validate. Fe(0)-N_x moiety in homogeneous molecules, e.g. iron(0) porphyrin, has been well known for efficiently catalyzing reduction reactions.[49] Here, the formed Fe(0) transition state with nitrogen coordination is probably analogous to the molecular unit. However, the very short lifetime of the active intermediate in an aqueous solution challenges the identification of its real structure by conventional spectroscopies, and thus requires future great efforts. Fe site densities with the transition of different oxidation states are further plotted in Fig. 2b as per the number of charges recorded at the plateau assigned to the Fe(II), assuming the total site number is constant. The redox behavior of Fe-N_x moiety shows more positive and narrower potential ranges for both Fe(III/II) and Fe(II/0) transformation than those of Fe NPs as displayed in Fig. S14d. This suggests the feature of the high reversibility of single-site transition-metal catalysts. In contrast, bulk metals may suffer from the surface passivation with poorly conductive oxides or hydroxides formation, resulting in lower electron mobility through surface layers. The iron

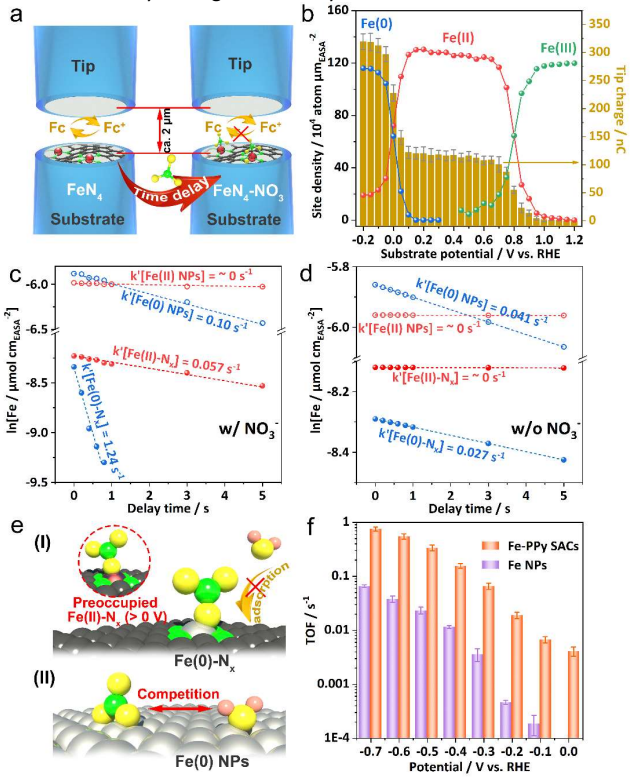

Fig. 3 SI-SECM for studying NitRR mechanism. (a) the schematic SI-SECM setup for the titration of Fe sites. (b) Electrochemically active surface area (EASA)-normalized active site density and corresponding titration charges of Fe-PPy SACs plotted against different potentials. The decay on Fe (II) and Fe (0) active site concentrations with different delay time in solution (c) with and (d) without NO_3^-. (e) The proposed preoccupied NitRR mechanism for the single-site center and classical competitive mechanism for the bulk surface. (f) TOFs of Fe-PPy SACs and Fe NPs based on the result of SI-SECM for ammonia production.

chemistry obtained in this study highlighted that the unique thermodynamic and kinetic properties may allow Fe-N_x SACs to catalyze a variety of reduction reactions with intrinsically improved activity.

In aqueous electrocatalysis, the on-site competition between water and substrate molecules, such as NO_3^-, substantially challenges the selectivity over objective products. The practical potentials required on metallic heterogeneous electrocatalysts for the NitRR are typically more negative than those needed for the HER, causing low faradaic efficiencies for the ammonia yield. One interesting finding as discussed is that the single-site iron can selectively reduce nitrate without the observable hydrogen evolution from water dissociation. We then attempted to seek insight into the HER and NitRR on isolated and bulk Fe sites with the SI-SECM, which can measure the kinetic behavior of two electrocatalytic reactions separately. Notably, NH_3 was detected at the potential above 0 V for the Fe-PPy SACs (Fig. 2b), where the Fe site had yet to be reduced to

the metallic state as per the titration result. However, no signals of the nitrate reduction like this at such positive potential were ever observed on Fe NPs. The time-delay titration of Fe(II) and Fe(0) at 0.2 V and -0.2 V was carried out in the nitrate solution. Fig. 3c exhibits the relationship between the surface concentration of Fe site, [Fe], and the delay time for Fe-PPy SAC and Fe NPs. Specifically, both single-atomic Fe(II)-N_x and Fe(0)-N_x were able to react with the NO_3^- as a result of the decay on [Fe] with the delay time after which the tip generated titrants. After linearly fitting the plots of ln[Fe] vs. delay time as the pseudo-first-order reaction, we obtained the reaction rates of the NO_3^- binding with Fe(II)-N_x and Fe(0)-N_x moieties were 0.057 and 1.24 s^{-1}. By comparison, Fe(II) transition state in Fe NPs shows no such catalytic activity, which is independent of the delay time. Instead, the nitrate adsorption was only observed when the Fe(0) formation on the surface with a much slower reaction rate of 0.01 s^{-1} than that of Fe-N_x. In the case of the HER, a similar SI-SECM experiment was conducted in the KOH solution with nitrate free. No signals of Fe(II) reacting with H_2O in both single-atom and nanoparticle catalysts have been ever seen in all independent trials, while Fe(0) can induce the water dissociation with the reaction rate of 0.027 and 0.041 s^{-1} for Fe-PPy SACs and Fe NPs.

The proactive Fe(II)-N_x toward the selective nitrate activation appears to be closely linked to the high faradaic efficiency of the ammonia production, which can eliminate the domination of water upon reaching negative potentials. Namely, NO_3^- is likely to preoccupy most Fe sites in Fe-PPy SACs at the Fe(II) transition state prior to the formation of Fe(0), the HER active center. In this case, even though nitrate-preoccupied Fe(II)-N_x experiences a further reduction to Fe(0)-N_x, the HER would be completely suppressed as a consequence of none or very few available adsorption sites for water molecules (Fig. 3e). Yet the behavior of the NitRR and HER on bulk Fe surface, like nanoparticles, is evidently different from the preoccupied site mechanism as demonstrated for Fe-PPy SACs. The oxidized Fe, such as Fe(II), is unlikely to react with either NO_3^- or water, which subsequently compete to be adsorbed on Fe(0) sites once the electrode potential can drive the reduction of Fe(II). This competition mechanism as displayed by Fe NPs is known for most aqueous electrocatalytic reactions of which potential overlays with the water splitting. In contrast to water, much lower concentration and slower mass transport of target substances essentially prohibit their binding with active sites in catalysts. Instead, the isolated Fe center in atomic distribution allows a preoccupied Fe(II)-N_x intermediate, where no water molecules are able to react with the catalyst. This suggests the unique coordination environment of SACs may adequately regulate the electronic structure of transition-metal atoms, thus significantly promoting the activity and selectivity that would be hardly achieved by bulk metals. Additionally, the proposed preoccupied mechanism would provide exciting opportunities to make it possible for highly selective electrocatalysis and electrosynthesis under full aqueous conditions.

The density of active sites that participate in the NitRR has been precisely quantified with the SI-SECM for Fe-PPy SACs and Fe NPs as shown in Fig. 3b and Fig. S14d, respectively. One would expect the turnover frequency (TOF, s^{-1}) to be calculated in order to further reveal the intrinsic activity. Here, TOF was estimated as per the site number and the yield rate of NH_3 at different potentials (see details in Experimental Section). Fig. 3f demonstrates the histograms of TOF vs. potentials for the number of ammonia molecules production per second on one Fe site in two as-prepared catalysts. Specifically, Fe-PPy SACs display the TOFs of 0.006 - 0.7 s^{-1} at potentials from 0 to -0.7 V while Fe NPs can only deliver the TOFs of 0.00015 - 0.06 s^{-1}. The result indicates at least twelve times higher rate on individual active sites is exhibited by the isolated Fe atoms compared with that of the bulk Fe surface. The experimental data we obtained with the assistance of the SI-SECM technique hopefully clarify the extraordinary selectivity and activity of single-atomic transition-metal catalysts for a particularly challenging reaction, converting nitrate ion to ammonia in water solution.

Theoretical understanding of electronic structures and NitRR mechanism

Density functional theory (DFT) calculations were conducted to help the understanding of the fundamental reason for the highly selective nitrate reduction displayed by Fe single-site catalyst. The charge density differences of Fe-N_4 and Fe bulk surface models to simulate the Fe-PPy SACs and Fe NPs after adsorbing NO_3^- are illustrated in Fig. 4a and b. For the isolated Fe atom, one O atom of NO_3^- is more likely to be adsorbed on the Fe site in the way of the end-on mode (the most favorable configuration) in accordance with the optimized geometric structure. However, two adjacent Fe atoms of Fe NPs appear to bond with two O atoms simultaneously in the form of the side-on mode. Besides, the sliced isosurface of charge distribution implies the iron site can serve as the nitrate-activated center in Fe-PPy SACs because of the accumulated (red) electron between Fe and

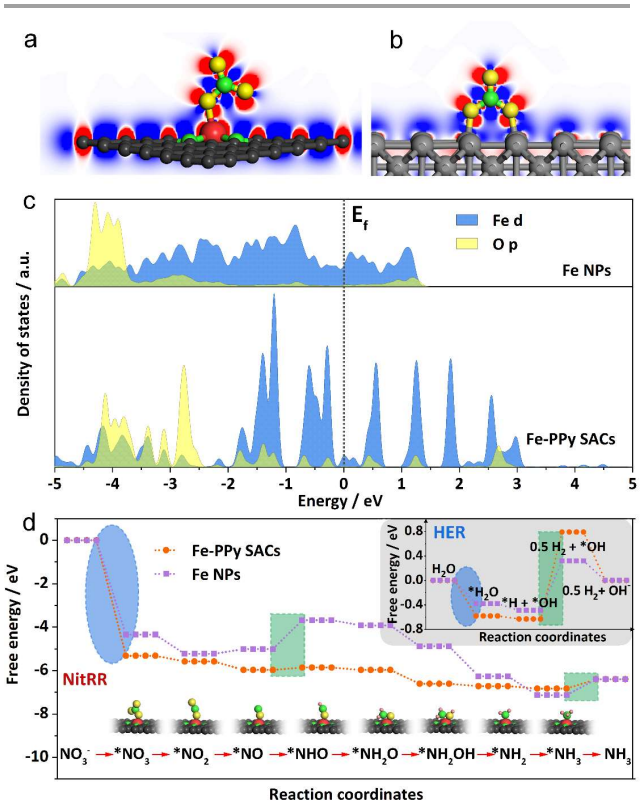

Fig. 4 DFT calculations. The optimized charge density difference of (a) Fe-PPy SACs and (b) Fe NPs after adsorbing NO_3^-. (c) PDOS of Fe d and

O p of NO_3^--bonded to Fe-PPy SACs and Fe NPs. (d) Gibbs free-energy diagram of nitrate reduction to ammonia and water dissociation (the top right).

O atoms. The partial density of states (PDOS) of Fe-PPy SACs and Fe NPs after bonding NO_3^- was further compared in Fig. 4c. Due to the isolated Fe atom, Fe d reveals the energy levels splitting and the electron density near the Fermi level (E_f) is dramatically decreased. The discrete electronic level is the typical feature of single atom materials,[50, 51] which greatly affecting the activation of the adsorbate. As a comparison, Fe d of Fe NPs is in a continuous state throughout E_f, suggesting the metallic feature. Adsorbed NO_3^- on Fe-PPy SACs is more active than that on Fe NPs as a result of the pronounced hybridization between O p and Fe d as well as the obvious overlap of electron density at the antibonding orbitals.

The Gibbs free-energy diagram further provides more details about the NitRR mechanism. We compared the first step of NitRR over Fe(II)-N_4, Fe(0), and Fe(II)-OH sites as shown in Fig. S16. The calculated free energy implies only Fe-N_4 and metallic Fe can adsorb NO_3^- spontaneously, while Fe(II)-OH is incapable, which is in agreement with the results of SI-SECM. As such, the following steps of NitRR were conducted with Fe-N_4 and metallic Fe models. The geometric structure of each intermediate (in the bottom of Fig. 4d) along NitRR steps was optimized prior to thermodynamic calculations.[52] The element steps as considered in this work are based on the previously reported mechanism, where the deoxygenation of nitrate takes place before the protonation process.[53, 54] Specifically, NO_3^- is first adsorbed to give $*NO_3$ with a dramatic energy decrease up to 5 eV for Fe-PPy SACs, implying the favorable NO_3^- adsorption. Then the N-O cleavage of $*NO_3$ produces $*NO_2$ and *NO step by step. Next, three continued protonation steps of *NO generate *NHO, $*NH_2O$, and $*NH_2OH$, respectively. The first protonation of *NO to *NHO requires to overcome a large energy barrier of 1.33 eV for Fe NPs, which suggests the Fe single site can facilitate the formation of *NHO. Subsequently, $*NH_2OH$ goes through another N-O cleavage and hydrogenation to form $*NH_3$. Finally, $*NH_3$ desorbs from the catalyst surface to produce free NH_3 via consuming energy of 0.43 and 0.73 eV for Fe-PPy SACs and Fe NPs. Overall, NitRR involves around night elementary steps and various intermediates, which is much more complicated than the competing HER with only three steps under alkaline conditions (as indicated in the top right of Fig. 4d). However, the free energy difference (ΔG) of NO_3^- adsorption on catalysts is much more negative than that of H_2O adsorption by about one order of magnitude, suggesting the Fe active site should be basically occupied by NO_3^- as we discussed in the previous section. For the Gibbs free-energy diagram of water dissociation, the desorption of *H is considered as the rate-determining step, where a larger ΔG (1.42 eV) is observed on Fe-PPy SACs indicates the inadequate HER activity compared with the iron bulk surface (ΔG = 0.81 eV). Namely, the isolated Fe sites are likely to outperform Fe nanoparticles with the more active adsorption of NO_3^-, the favorable formation of *NHO, and suppression of the competition from the HER.

Conclusions

Endowed with unique coordination state and electronic structure, atomically dispersed iron sites on carbon matrix demonstrated considerably improved activity and selectivity for the nitrate electro-reduction to ammonia. In comparison to Fe NPs, the reported Fe-PPy SACs deliver 12 times higher TOF with nearly 100% faradaic efficiency for NH_3 production. The analysis of by-products in the presence of NO_3^- reveals no obvious H_2 gas was ever detected for single-site Fe catalysts, while significant water dissociation was observed on both bulk Fe surface (Fe NPs) and carbon support at negative potentials. In situ mechanistic study found the exclusive existence of nitrate-preoccupied Fe(II)-N_x sites prior to the Fe(0) formation, which can effectively eliminate the competing water adsorption under aqueous conditions. Given the fact that localized states of isolated transition-metal atoms are closely relevant to redox and kinetic behaviors, one would expect regulating the coordination environment to allow single-atom catalysts with distinguished performance. The present findings also show promise of nitrogen pollution management through the electrocatalytic approach of using single-site iron catalysts, thus contributing in several ways to the future sustainability of fertilizer and renewable fuels recycling.

Conflicts of interest

There are no conflicts to declare.

Acknowledgements

G.Y. acknowledges the funding support from the U.S. Department of Energy, Office of Science, Basic Energy Sciences under Award DE-SC0019019, and Camille Dreyfus Teacher-Scholar Award. We especially thank Prof. Allen J. Bard group for the support on scanning electrochemical microscopy and constructive discussion.

References

1. *U.S. Geological Survey*, 2020, 116.
2. J. N. Galloway, A. R. Townsend, J. W. Erisman, M. Bekunda, Z. Cai, J. R. Freney, L. A. Martinelli, S. P. Seitzinger and M. A. Sutton, *Science*, 2008, **320**, 889-892.
3. J. W. Erisman, M. A. Sutton, J. Galloway, Z. Klimont and W. Winiwarter, *Nat. Geosci.*, 2008, **1**, 636-639.
4. A. Valera-Medina, H. Xiao, M. Owen-Jones, W. I. F. David and P. J. Bowen, *Prog. Energy Combust. Sci.*, 2018, **69**, 63-102.
5. C. H. Christensen, T. Johannessen, R. Z. Sørensen and J. K. Nørskov, *Catal. Today*, 2006, **111**, 140-144.
6. *Institute for Industrial Productivity*, http://www.iipinetwork.org/wp-content/letd/content/ammonia.html.
7. G. Zheng, J.-M. Yan and G. Yu, *Small Methods*, 2019, **3**, 1900070.
8. P. Li, Z. Jin, Z. Fang and G. Yu, *Angew. Chem. Int. Ed.*, 2020, **59**, 22610-22616.
9. C. Lv, Y. Qian, C. Yan, Y. Ding, Y. Liu, G. Chen and G. Yu, *Angew. Chem. Int. Ed.*, 2018, **57**, 10246-10250.
10. C. Lv, L. Zhong, Y. Yao, D. Liu, Y. Kong, X. Jin, Z. Fang, W. Xu, C. Yan, K. N. Dinh, M. Shao, L. Song, G. Chen, S. Li, Q. Yan and G. Yu, *Chem*, 2020, **6**, 2690-2702.
11. Z. Fang, D. Fernandez, N. Wang, Z. Bai and G. Yu, *Sci. China Chem.*, 2020, **63**, 1570-1577.

12. D. R. Kanter, O. Chodos, O. Nordland, M. Rutigliano and W. Winiwarter, *Nat. Sustain.*, 2020, **3**, 956-963.
13. G. P. Robertson and P. M. Vitousek, *Annu. Rev. Environ. Resour.*, 2009, **34**, 97-125.
14. X. Zhang, E. A. Davidson, D. L. Mauzerall, T. D. Searchinger, P. Dumas and Y. Shen, *Nature*, 2015, **528**, 51-59.
15. G.-F. Chen, Y. Yuan, H. Jiang, S.-Y. Ren, L.-X. Ding, L. Ma, T. Wu, J. Lu and H. Wang, *Nat. Energy*, 2020, **5**, 605-613.
16. P. H. Van Langevelde, I. Katsounaros and M. T. M. Koper, *Joule*, 2021, **5**, 290-294.
17. P. Lam and M. M. M. Kuypers, *Ann. Rev. Mar. Sci.*, 2011, **3**, 317-345.
18. Y. Wang, A. Xu, Z. Wang, L. Huang, J. Li, F. Li, J. Wicks, M. Luo, D.-H. Nam, C.-S. Tan, Y. Ding, J. Wu, Y. Lum, C.-T. Dinh, D. Sinton, G. Zheng and E. H. Sargent, *J. Am. Chem. Soc.*, 2020, **142**, 5702-5708.
19. H. Niu, Z. Zhang, X. Wang, X. Wan, C. Shao and Y. Guo, *Adv. Funct. Mater.*, 2020, 2008533.
20. S. Ji, Y. Chen, X. Wang, Z. Zhang, D. Wang and Y. Li, *Chem. Rev.*, 2020, **120**, 11900-11955.
21. S. K. Kaiser, Z. Chen, D. Faust Akl, S. Mitchell and J. Pérez-Ramírez, *Chem. Rev.*, 2020, **120**, 11703-11809.
22. L. Wang, W. Zhang, S. Wang, Z. Gao, Z. Luo, X. Wang, R. Zeng, A. Li, H. Li, M. Wang, X. Zheng, J. Zhu, W. Zhang, C. Ma, R. Si and J. Zeng, *Nat. Commun.*, 2016, **7**, 14036.
23. Y. Pan, R. Lin, Y. Chen, S. Liu, W. Zhu, X. Cao, W. Chen, K. Wu, W.-C. Cheong, Y. Wang, L. Zheng, J. Luo, Y. Lin, Y. Liu, C. Liu, J. Li, Q. Lu, X. Chen, D. Wang, Q. Peng, C. Chen and Y. Li, *J. Am. Chem. Soc.*, 2018, **140**, 4218-4221.
24. Z. Jin and A. J. Bard, *Proc. Natl. Acad. Sci.*, 2020, **117**, 12651-12656.
25. T. Zhu, Q. Chen, P. Liao, W. Duan, S. Liang, Z. Yan and C. Feng, *Small*, 2020, **16**, 2004526.
26. H. Zheng, G. Wisedchaisri and T. Gonen, *Nature*, 2013, **497**, 647-651.
27. J. M. Vega and H. Kamin, *J. Biol. Chem.*, 1977, **252**, 896-909.
28. M. Hirasawa, J. N. Tripathy, F. Sommer, R. Somasundaram, J.-S. Chung, M. Nestander, M. Kruthiventi, M. Zabet-Moghaddam, M. K. Johnson, S. S. Merchant, J. P. Allen and D. B. Knaff, *Photosynth. Res.*, 2010, **103**, 67-77.
29. J. Bo, X. Luo, H. Huang, L. Li, W. Lai and X. Yu, *J. Power Sources*, 2018, **407**, 105-111.
30. G. Wu, K. L. More, C. M. Johnston and P. Zelenay, *Science*, 2011, **332**, 443-447.
31. Z. Fang, P. Li and G. Yu, *Adv. Mater.*, 2020, **32**, 2003191.
32. Y. Guo, J. Bae, Z. Fang, P. Li, F. Zhao and G. Yu, *Chem. Rev.*, 2020, **120**, 7642-7707.
33. X. Li, X. Chen, Z. Jin, P. Li and D. Xiao, *Mater. Chem. Front.*, 2021, **5**, 1140-1163.
34. D. P. Malenov and S. D. Zarić, *Coord. Chem. Rev.*, 2020, **419**, 213338.
35. P. Li, Z. Jin and D. Xiao, *J. Mater. Chem. A*, 2017, **5**, 3274-3283.
36. Z. Jin, P. Li, Y. Jin and D. Xiao, *Energy Storage Mater.*, 2018, **13**, 160-167.
37. P. Li, Z. Jin, Y. Qian, Z. Fang, D. Xiao and G. Yu, *ACS Energy Lett.*, 2019, **4**, 1793-1802.
38. Q. Jia, N. Ramaswamy, H. Hafiz, U. Tylus, K. Strickland, G. Wu, B. Barbiellini, A. Bansil, E. F. Holby, P. Zelenay and S. Mukerjee, *ACS Nano*, 2015, **9**, 12496-12505.
39. Y. J. Sa, J. H. Kim and S. H. Joo, *J. Electrochem. Sci. Technol*, 2017, **8**, 169-182.
40. J. Li, S. Ghoshal, W. Liang, M.-T. Sougrati, F. Jaouen, B. Halevi, S. McKinney, G. McCool, C. Ma, X. Yuan, Z.-F. Ma, S. Mukerjee and Q. Jia, *Energy Environ. Sci.*, 2016, **9**, 2418-2432.
41. N. Zhang, T. Zhou, M. Chen, H. Feng, R. Yuan, C. a. Zhong, W. Yan, Y. Tian, X. Wu, W. Chu, C. Wu and Y. Xie, *Energy Environ. Sci.*, 2020, **13**, 111-118.
42. N. Zhang, T. Zhou, J. Ge, Y. Lin, Z. Du, C. a. Zhong, W. Wang, Q. Jiao, R. Yuan, Y. Tian, W. Chu, C. Wu and Y. Xie, *Matter*, 2020, **3**, 509-521.
43. M. Kitano, Y. Inoue, M. Sasase, K. Kishida, Y. Kobayashi, K. Nishiyama, T. Tada, S. Kawamura, T. Yokoyama, M. Hara and H. Hosono, *Angew. Chem. Int. Ed.*, 2018, **57**, 2648-2652.
44. X.-W. Guo, S.-M. Chen, H.-J. Wang, Z.-M. Zhang, H. Lin, L. Song and T.-B. Lu, *J. Mater. Chem. A*, 2019, **7**, 19831-19837.
45. F. Simpson and R. Burris, *Science*, 1984, **224**, 1095-1097.
46. P. Li, Z. Jin, Y. Qian, Z. Fang, D. Xiao and G. Yu, *Mater. Today*, 2020, **35**, 78-86.
47. Z. Jin and A. J. Bard, *Angew. Chem. Int. Ed.*, 2021, **60**, 794-799.
48. H. Kim, W. Yang, W. H. Lee, M. H. Han, J. Moon, C. Jeon, D. Kim, S. G. Ji, K. H. Chae, K.-S. Lee, J. Seo, H.-S. Oh, H. Kim and C. H. Choi, *ACS Catal.*, 2020, **10**, 11674-11684.
49. I. Bhugun, D. Lexa and J.-M. Savéant, *J. Am. Chem. Soc.*, 1996, **118**, 3982-3983.
50. M. Boronat, A. Leyva-Pérez and A. Corma, *Acc. Chem. Res.*, 2014, **47**, 834-844.
51. Y. Sun, J. Wang, Q. Liu, M. Xia, Y. Tang, F. Gao, Y. Hou, J. Tse and Y. Zhao, *J. Mater. Chem. A*, 2019, **7**, 27175-27185.
52. S. Garcia-Segura, M. Lanzarini-Lopes, K. Hristovski and P. Westerhoff, *Appl. Catal., B*, 2018, **236**, 546-568.
53. Y. Wang, W. Zhou, R. Jia, Y. Yu and B. Zhang, *Angew. Chem. Int. Ed.*, 2020, **59**, 5350-5354.
54. R. Jia, Y. Wang, C. Wang, Y. Ling, Y. Yu and B. Zhang, *ACS Catal.*, 2020, **10**, 3533-3540.